Nature Communications

https://doi.org/10.1038/s41467-026-70924-z

Article in Press

Spatiotemporally engineered tumor-derived extracellular vesicle-based scaffold vaccine for personalized cancer immunotherapy

Received: 23 April 2025

Accepted: 6 March 2026

Cite this article as: Chen, Q., Jiang, C., Du, X. *et al.* Spatiotemporally engineered tumor-derived extracellular vesicle-based scaffold vaccine for personalized cancer immunotherapy. *Nat Commun* (2026). https://doi.org/10.1038/s41467-026-70924-z

Qi Chen, Chenwei Jiang, Xinxing Du, Minglu Tang, Qi Shang, Cong Hu, Zehong Peng, Wei Xue, Liang Dong, Feihu Wang & Jiahua Pan

Spatiotemporally Engineered Tumor-derived extracellular vesicle-based scaffold vaccine for personalized cancer immunotherapy

Qi Chen[1#], Chenwei Jiang[2#], Xinxing Du[1], Minglu Tang[2], Qi Shang[2], Cong Hu[1], Zehong Peng[1], Wei Xue[1]*, Liang Dong[1]*, Feihu Wang[2]*, Jiahua Pan[1]*

[1]Department of Urology, Renji Hospital, Shanghai Jiao Tong University School of Medicine, Shanghai, 200127, China.
[2]School of Biomedical Engineering, Shanghai Jiao Tong University, Shanghai, 200241, China.
[#]QC and CJ contributed equally to this work.

*Correspondence to: WX, uroxuewei@163.com; LD, drdongliang@126.com; FW, fhwang21@sjtu.edu.cn; JP, panjiahua@renji.com.

Abstract: Personalized vaccines demonstrate remarkable potential in leveraging tumor-specific adaptive immunity for cancer therapy. Nevertheless, current platforms face persistent challenges including premature systemic clearance and imprecise antigen-presenting cell targeting, culminating in transient and inefficient antitumor immunity. Furthermore, the technical complexity, extended timelines, and prohibitive costs required for tumor-specific neoantigen identification continue to impede the clinical translation of personalized cancer vaccines. Here, we report a tumor-derived extracellular vesicle-based scaffold vaccine that elicits robust and durable antitumor immunity for personalized cancer immunotherapy. Following subcutaneous administration, the *in situ*-formed hydrogel vaccine serves as a sustained reservoir for tumor-derived extracellular vesicle antigens and adjuvants while recruiting antigen-presenting dendritic cells to accumulate within the scaffold. Upon exposure to this antigen-rich depot, immature dendritic cells undergo efficient activation, with subsequently matured dendritic cells migrating to draining lymph nodes, where they induce potent and persistent tumor-specific $CD8^+$ T-cell responses that suppress tumor progression across multiple murine models. Specifically, when using tumor-derived extracellular vesicles isolated from surgically excised tumor tissues, the patient-tailored vaccines demonstrate remarkable efficacy in preventing postoperative recurrence. Our findings validate the robust and durable therapeutic efficacy of this vaccine platform, highlighting its potential as a customizable strategy for personalized cancer immunotherapy.

INTRODUCTION

Cancer vaccines represent a paradigm-shifting immunotherapeutic strategy that activates tumor-specific adaptive immunity for precise malignant cell targeting, demonstrating transformative potential to redefine modern oncology frameworks[1–4]. Personalized cancer vaccines utilize systematically characterized tumor mutanomes to engineer neoantigen-based formulations, which elicit tumor-selective T-cell responses through optimized epitope prioritization[5–7]. Despite this promise, current personalized cancer vaccines show suboptimal clinical efficacy, with merely three FDA-approved formulations demonstrating limited therapeutic benefits[8]. These immunogenic limitations stem from rapid mononuclear phagocyte system-mediated clearance of conventional delivery platforms and insufficient antigen accumulation in lymph nodes[9]. While passive drainage enables partial vaccine component access to lymphatics, inadequate antigen retention and disorganized spatial distribution critically compromise dendritic cell-mediated capture and processing cascades, ultimately leading to transient T-cell activation and inadequate antitumor immunity[10]. Moreover, the neoantigen discovery pipeline—encompassing tumor antigen screening, computational prediction, and experimental validation in individual patients—constitutes a multidimensional, resource-intensive process that critically impedes the clinical translation of personalized cancer vaccines[11–13]. To overcome these barriers, systematic engineering of neoantigen acquisition coupled with rationally designed antigen-presenting cell -targeted delivery platforms represents imperative to unlock the full clinical potential of this precision immunotherapy.

Extracellular vesicles (EVs), naturally secreted nanoscale vesicles with lipid bilayer architectures, faithfully mirror the molecular signatures of their parental cells[14–16]. Tumor-derived extracellular vesicles (TEVs) serve as natural reservoirs of tumor-associated antigens, including neoantigens that evade conventional identification methods[17–19]. Our protein level validation in prostate cancer surgical specimens revealed preserved antigenic profiles in TEVs, demonstrating equivalent expression levels of prostate-specific antigens (PAP, PSCA, PSMA) between TEVs and matched tumor lysates (Fig. 1, A and B). Furthermore, a protease protection assay confirmed that these antigens are predominantly localized on the surface of TEVs (Supplementary Fig. 1). Mechanistically, TEVs coordinate patient-specific antitumor immunity through intrinsic delivery of individualized neoantigen repertoires[6,20,21]. Clinically, autologous TEVs could be isolated from surgical specimen, which bypass computational neoantigen prediction through comprehensive antigen payloads, enabling accelerated personalized vaccine manufacturing. TEV-based vaccines thus represent a breakthrough platform in precision immunotherapy by leveraging biomimetic carriers of tumor-specific antigens. However, TEVs are susceptible to rapid clearance by the mononuclear phagocyte system, while their suboptimal size distribution hinders effective

lymphatic transport, thereby significantly restricting their therapeutic potential[10,22]. We therefore propose that spatiotemporal reprogramming of TEVs' biodistribution to sustain antigen-presenting cell interactions will elicit robust and durable tumor-specific immunity.

Notably, peptide-based supramolecular hydrogels have emerged as a transformative drug delivery platform due to their inherent biosafety, biocompatibility, and multifunctionality[23–26]. These biomaterials demonstrate exceptional depot functionality by enabling enhanced local drug retention coupled with controlled release kinetics, thus maximizing therapeutic bioavailability at the target site[27–29]. Our recent work has established their unique suitability for localized delivery of immune modulators, with payload release significantly prolonged through electrostatic interactions[30–32]. Specifically, engineered hydrogel scaffolds can reconstruct lymph-node-mimicking immune niches - three-dimensional microenvironments where interconnected macroporous networks facilitate immune cell infiltration, interaction, and dissemination[33,34]. Building on this premise, we propose that hydrogel-based antigen/adjuvant depots, while recruiting dendritic cells (DCs) to accumulate within the scaffold, enable enhanced DC uptake efficiency through sustained exposure to abundant payloads. Following maturation, these DCs migrate to lymph nodes to activate T-cell responses. This paradigm-shifting strategy overcomes conventional vaccine limitations via spatiotemporal reprogramming of antigen/adjuvant biodistribution, thereby extending DC-antigen engagement duration and amplifying antitumor immunity through coordinated immune modulation.

In this context, we develop a TEVs-based scaffold vaccine for personalized cancer immunotherapy and demonstrated the system's high potency in eliciting robust and durable immunity against tumor regression (Fig.1C). The vaccine components- TEVs and adjuvant 2'3'-c-di-AM(PS)$_2$ (CDA), along with the granulocyte-macrophage colony-stimulating factor (GM-CSF) for dendritic cell recruitment - are integrated onto self-assembling FK12 peptide nanofibers (FK$_{12}$F). Following subcutaneous injection, the TCG/FK$_{12}$F complex rapidly transforms into a hydrogel vaccine that serves as a localized depot, substantially extending the retention duration of immunotherapeutic agents. The scaffold facilitates antigen-presenting DCs recruitment and concentration, enabling immature DCs to capture and process TEV antigens with CDA adjuvant support, thereby promoting DC maturation. These antigen-primed mature DCs then migrate to draining lymph nodes, initiating potent tumor-specific CD8$^+$ T-cell activation that confers long-term antitumor protection. Our results demonstrate that the personalized TCG/FK$_{12}$F vaccine effectively suppresses postoperative tumor recurrence and enhances overall survivals in both RM-1 prostate cancer and 4T1 breast cancer models.

RESULTS

Characterization of TCG/$FK_{12}F$ hydrogel vaccine

To construct a biocompatibility and biodegradability hydrogel scaffold, a self-assembling peptide FKFEFKFEGRGD (FK_{12}) was the synthesized (Supplementary Fig. 2). This amphiphilic molecule is capable of self-assembling into regular and homogeneous nanofibers ($FK_{12}F$) in aqueous solutions, which can subsequently intertwine to form supramolecular hydrogels under physiological conditions (Fig. 2A). We then simulated the *in vivo* environment by adding counterions (PBS or serum) to the $FK_{12}F$ aqueous solution, and found that the originally flowing solution immediately transformed into a self-supporting hydrogel (Fig. 2B and Supplementary Fig. 3A). Rheological tests corroborated this observation, as the storage modulus (G') rapidly exceeded the loss modulus (G") upon PBS or serum addition (Fig. 2C and Supplementary Fig. 3B), indicative of a phase transition and enhanced elastic properties.

TEVs were obtained from culture medium supernatants of RM-1 prostate cancer cells to prepare vaccine for subsequent experiments. Transmission electron microscopy revealed that the extracted TEVs showed a characteristic cup-shaped morphology (Fig. 2D). The results of nanoflow analysis showed that the particle size distribution of the TEVs was within the 30-160 nm interval (Fig. 2E). Western blot analysis of TEVs compared with RM-1 cell lysates (CLs) demonstrated negligible expression of the contaminant protein Calnexin, Apoa-1 and GM130 in TEVs, alongside positive expression of extracellular vesicle markers Flotillin-1, CD63, and CD9 (Fig. 2F and Supplementary Fig. 4). These findings collectively confirm the successful isolation of TEVs from RM-1 cells. To prepare vaccine preparations, we mixed negatively charged GM-CSF, CDA and TEVs with positively charged $FK_{12}F$. The decrease in the Zeta potential of the solution after loading the vaccine components suggests that the components were successfully condensed on the surface of $FK_{12}F$ by electrostatic interaction (Fig. 2G). Meanwhile, confocal microscopy revealed a uniform distribution of TEVs within $FK_{12}F$, confirming their effective incorporation (Fig. 2H). Similar experimental results showed that $FK_{12}F$ loaded with vaccine components retained its capacity to form a gel in the presence of PBS (Supplementary Fig. 2, D).

The release of GM-CSF and CDA from the TCG/$FK_{12}F$ hydrogel was subsequently investigated *in vitro* at 37°C. We observed that both components showed a nonlinear sustained slow release (Fig.2I). Within 13 d GM-CSF released 51% while CDA released 80%. This nonlinear release profile is characteristic of therapeutic agents encapsulated within hydrogels, where the release rate decreases over time after an initial abrupt release. We then evaluated the biodegradation of $FK_{12}F$ *in vivo* by subcutaneous injection of $FK_{12}F$ solution into the back of C57/BL6 mice. 15 minutes after injection, we euthanized the

mice and could observe that the injected $FK_{12}F$ solution had formed a well-defined spherical gel. The in situ-formed $FK_{12}F$ hydrogel demonstrated gradual biodegradation over 15 days (Supplementary Fig. 5).

To further assess the potential of $FK_{12}F$ hydrogels as drug reservoirs, we investigated subcutaneous therapeutic release behavior in mice using Cy7-labeled CDA and DIR-labeled TEVs, respectively. The fluorescently labeled CDA and TEVs were mixed with $FK_{12}F$ aqueous solution, respectively, and the mixed solution were subsequently injected subcutaneously into mice; free Cy7-labeled CDA and DIR-labeled TEVs were used as controls. *In vivo* fluorescence imaging revealed that both CDA and TEVs in the $FK_{12}F$ hydrogel exhibited strong localized signals at the injection site and negligible accumulation in major organs (liver, spleen, kidney, heart, and lung) (Fig. 2J, K and Supplementary Fig. 6). This indicates that the vaccine components were effectively retained locally without systemic dissemination. As envisaged, the fluorescence intensity of free CDA and TEVs declined rapidly with time, and fluorescence was barely detectable after 5 days. In contrast, the $FK_{12}F$-treated group still remained strong fluorescent intensity through day 15 (Fig. 2, J and K). These results further demonstrated that the $FK_{12}F$ hydrogel can serve as a therapeutic reservoir, significantly extending the local release time of the vaccine components. Moreover, hematoxylin eosin staining of major organs, complete blood counts, serum biochemistry, and cytokine analysis showed no significant differences between TCG/FK12F-treated mice compared to healthy controls (Supplementary Fig. 7). Specifically, serum IL-6 levels were comparable to those in healthy mice (Supplementary Fig. 8), indicating that localized TCG/$FK_{12}F$ administration does not induce systemic inflammation and exhibits a favorable safety profile.

TCG/$FK_{12}F$ activates DCs *in situ* and enhancing lymph node migration for adaptive immunity

To investigate the underlying mechanism of the vaccine, we surgically removed the subcutaneous gel implants after a designated period and performed flow cytometric analysis. By directly comparing the effects of TLs and TEVs on DC activation, we found that in the absence of CDA, TEVs did not markedly enhance the expression of co-stimulatory molecules CD80/CD86 on DCs relative to TLs, however, they induced a significantly higher level of MHC I expression (Supplementary Fig. 9). These data indicate that, although TEVs alone are insufficient to drive full DC maturation, they possess superior antigen-presenting potential compared with TLs. Notably, a significant higher number of DCs were detected in the TCG/$FK_{12}F$ group compared to the $FK_{12}F$ and CG/$FK_{12}F$ groups (Fig. 3A). To further delineate infiltrating DC subsets, we quantified conventional DCs (cDCs), monocyte-derived DCs (moDCs), and plasmacytoid DCs (pDCs) by flow cytometry. Compared to the $FK_{12}F$ group, the CG/$FK_{12}F$ formulation enhanced the abundance of cDC1s and moDCs (Supplementary Fig. 10), indicating that the adjuvant

potentiates the recruitment of these functionally critical DC subsets. Furthermore, the TCG/FK_{12}F vaccine significantly increased the percentages of cDC1s, cDC2s, and moDCs within the hydrogel relative to control groups. Meanwhile, the proportion of activated DCs in the TCG/FK12F group was 4-fold and 1.6-fold higher than in the FK12F and CG/FK12F groups, respectively (Fig. 3B). Furthermore, DCs in this group showed significantly elevated expression of the CCR7 receptor (Fig. 3C), a key mediator of lymph node migration. Accordingly, inguinal lymph nodes of TCG/FK_{12}F-immunized mice exhibited 2.8-fold and 1.9-fold increases in activated DCs compared to those from FK_{12}F- and CG/FK_{12}F-treated mice, respectively (Fig. 3D). Importantly, TCG/FK_{12}F induced significantly higher percentage of $CD4^+$ (21.4%) and $CD8^+$ (16.3%) T cells compare with the FK_{12}F (14.2% and 12.5%) and CG/FK_{12}F (15.1% and 13.7%) treatment groups (Fig. 3E and F).

Furthermore, using an OVA-expressing RM-1 tumor model (Supplementary Fig. 11), we assessed antigen-specific immunity induced by the TEV-based hydrogel vaccine. Flow cytometry revealed that vaccination significantly upregulated MHC class I on DCs both within the hydrogel and in draining lymph nodes (Fig. 3G, H and Supplementary Fig. 12). This was accompanied by a marked increase in OVA-specific DCs (Fig. 3I), confirming efficient antigen delivery and antigen-dependent DC activation. In parallel, we observed a substantial expansion of SIINFEKL–H-$2K^b$ $tetramer^+$ $CD8^+$ T cells in draining lymph nodes, and splenocytes from vaccinated mice exhibited increased frequencies of IFN-γ^+ $CD8^+$ T cells upon *ex vivo* OVA restimulation (Fig. 3J and K). Together, these data demonstrate that the hydrogel vaccine promotes robust antigen-specific DC activation and primes a functional antigen-specific $CD8^+$ T-cell response. Collectively, our results robustly support that TCG/FK12F, as an efficient hydrogel vaccine scaffold system, facilitates DCs recruitment, maturation, and lymph node homing, thereby successfully initiating a potent adaptive anti-tumor immune response (Fig. 3L).

TCG/FK_{12}F vaccine elicits robust tumor-specific immunity to suppresses tumors

To evaluate the therapeutic efficacy of the vaccine initially, we established a subcutaneous tumor model using the murine prostate cancer cell line RM-1. When tumors reached 100-150 mm^3, mice were randomized into treatment groups, and the vaccine was injected by subcutaneously into the contralateral side of the tumor to evaluate the TCG/FK_{12}F vaccine and its synergistic anti-tumor effect with the immune checkpoint inhibitor aPD-1 (Fig. 4A). The results showed that the TCG/FK_{12}F group and the combined treatment group (TCG/FK_{12}F+aPD-1) significantly suppressed subcutaneous tumor growth and significantly prolonged the survival time of mice (Fig. 4B and C). In particular, 62.5% of mice in the combined treatment group remained alive at day 60, whereas the aPD-1, /FK_{12}F, and ree TCG groups

exhibited minimal improvements in survival. To dissect the changes in immune infiltration in the TME after different treatments, tumors were collected ten days after treatment for flow cytometry and cytokine assays. The results show that TCG/FK_{12}F vaccine treatment significantly elevated the infiltration of $CD8^+$ T cells and $CD8^+$ IFN-γ^+ T cells in TME, which was further enhanced by combining with aPD-1 (Fig. 4, D and E). Likewise, antitumor-associated cytokines were up-regulated in varying proportions (Fig. 4F and Supplementary Fig. 13, A to E). Consistent with the therapeutic outcomes, aPD-1 and CG/FK_{12}F treatment alone helped minimally to elevate immune infiltration, while free TCG also failed to demonstrate a significant effect, probably due to its limited *in vivo* retention.

To assess whether vaccine-activated T cells exhibit antigen specificity, splenocytes of mice were harvested 10 days after vaccination and incubated with TEVs (from RM-1 cells) for 24 hours. Enzyme-linked immunospot (ELISpot) assay was used to assess Interferon-γ (IFN-γ) secret from mice T cells after exposure to tumor antigens in different groups. Minimal IFN-γ-positive spots were detected in the PBS and CG/FK_{12}F groups, indicating that adjuvant alone elicits negligible antigen-specific T-cell activation (Fig. 4G and H). In the TCG treated group, a moderate number of T cells were activated, and this weak immune response may result from the limited duration of vaccine action. The TCG/FK_{12}F treated group exhibited a significantly higher frequency of IFN-γ-positive spots than the other groups, underscoring its superior capacity to activate antigen-specific T cells. Furthermore, to confirm that the therapeutic effect depends on TEV-specific antigens, we generated a control vaccine (T_{B16}CG/FK_{12}F) using TEVs from heterologous B16 cells. As shown in Supplementary Fig. 14, this control vaccine lacked significant efficacy, supporting the antigen-specific mechanism of action. These results strongly demonstrate that $CD8^+$ T cells respond to TEVs restimulation in a tumor antigen-specific way. To further delineate the contributions of T-cell subsets to vaccine efficacy, we depleted $CD4^+$ or $CD8^+$ T cells in RM-1 tumor-bearing mice using specific antibodies. Depletion of $CD4^+$ T cells partially impaired the antitumor effect of TCG/FK_{12}F, whereas clearance of $CD8^+$ T cells significantly reduced tumor growth inhibition (Supplementary Fig. 15 and Fig. 4I). These results confirm the positive effect of the TCG/FK_{12}F vaccine on the tumor immune microenvironment, suggesting that the efficacy of the vaccine is attributable to a robust immune response.

Surviving mice were rechallenged on day 60 by injecting tumor cells into the contralateral flank to assess whether TCG/FK_{12}F vaccine established a long-term immune memory (Fig. 4A). Meanwhile, we used untreated naive mice as a control group. As shown in Fig. 4J, naive mice were able to observe significant tumor development after inoculation and continued to grow over time. In contrast, almost no

detectable tumors were observed in mice from the previous long-term survival group, suggesting sustained resistance to tumor rechallenge. Meanwhile, these mice maintained a 100% survival rate through day 120 (Fig. 4K). To further investigate the underlying immune mechanisms, we euthanized previously long-surviving mice on day 120 and extracted lymphocytes from the spleen for flow cytometry analysis. We found both $CD8^+CD44^{high}CD62L^{high}$ central memory T (T_{cm}) cells and $CD8^+CD44^{high}CD62L^{low}$ effector memory T (T_{em}) cells were elevated in the TCG/FK_{12}F+aPD-1-treated group of mice compared to naive mice (Supplementary Fig. 16 and Fig. 4L and M). This suggests that the vaccine induced T-cell memory immunity and established long-term immunity to curb tumor recurrence.

TCG/FK_{12}F significantly suppresses proliferation in orthotopic prostate cancer and metastasis in 4T1 breast cancer

Since prostate cancer is characterized as an immunologically cold tumor, we constructed an orthotopic model mouse of prostate cancer to more accurately replicate the tumor microenvironment and evaluate the efficacy of the vaccine. We subcutaneously injected the vaccine preparations on day five after the *in situ* injection of RM-1 cells into the mouse prostate. We then assessed the therapeutic efficacy of the vaccine using tumor bioluminescence imaging and by monitoring survival (Fig. 5A). As shown in Fig. 5B and Supplementary Fig. 17, treatment with the TCG/FK_{12}F vaccine not only significantly inhibited tumor progression but also showed a further enhanced therapeutic effect when combined with aPD-1 therapy. Correspondingly, the two groups exhibited markedly prolonged survival compared to the PBS and CG/FK_{12}F groups (Fig. 5C). The mice were euthanized on day 15 and the tumors were obtained by autopsy. Both groups of mice demonstrated better tumor inhibition similarly (Fig. 5D and Supplementary Fig. 18). Flow cytometry analysis of orthotopic tumor tissues revealed higher infiltration of $CD8^+$ T cells and $CD8^+$ IFN-γ^+ T cells in the TCG/FK_{12}F and TCG/FK_{12}F + aPD-1 groups compared to the other groups (Supplementary Fig. 19 and 20). Consistent with this, immunohistochemistry and immunofluorescence analyses revealed increased $CD8^+$ T-cell infiltration and a higher abundance of granzyme B^+ cytotoxic T cells, respectively, in tumors receiving TCG/FK_{12}F combined with aPD-1 (Fig. 5E and Supplementary Fig. 21). In addition, immunofluorescence staining revealed elevated PD-1 expression on tumor-infiltrating $CD8^+$ T cells following vaccination (Supplementary Fig. 22), suggesting that sustained immune activation induced a state of partial T-cell exhaustion. This finding provides a mechanistic rationale for the enhanced therapeutic benefit achieved upon combination with immune checkpoint blockade. Furthermore, in the OVA-expressing RM-1 orthotopic model, flow cytometry demonstrated a significant increase in H-$2K^b$–OVA $tetramer^+$ $CD8^+$ T cells within tumor tissues following TCG/FK_{12}F

vaccination (Supplementary Fig. 23), indicating robust antigen-specific cytotoxic T-cell activation in the tumor microenvironment. Additionally, cytokine detection in tumor tissues showed a marked elevation of anti-tumor cytokines—including IFN-α, IFN-β, IFN-γ, TNF-α, and IL-6—in these two groups compared to the others (Fig. 5F), underscoring the vaccine's capacity to modulate the tumor immune microenvironment effectively.

Considering that tumor metastasis is a major cause of death in patients with advanced tumors, we evaluated the efficacy of the TCG/FK_{12}F vaccine in suppressing metastasis. To monitor tumor metastasis in mice, we used luciferase-labeled 4T1 cells to establish a systemic metastasis model by injecting these cells into the left ventricle of mice (Fig. 5G). We administered vaccine and other group treatments on the seventh day after cell injection. Bioluminescence imaging showed that by day 15, the PBS and aPD-1 group developed extensive systemic metastases and progressive mortality, whereas the TCG/FK_{12}F and TCG/FK_{12}F + aPD-1 mice displayed significantly attenuated disease progression, with metastatic burden in the TCG/FK_{12}F + aPD-1 group being almost exclusively confined to the lungs (Fig. 5, H and I). After euthanasia, peripheral blood, spleen, and lung tissues were collected for analysis. Flow cytometry of peripheral blood revealed a marked increase in circulating IFN-γ^+ $CD8^+$ T cells in TCG/FK_{12}F-treated mice (Supplementary Fig. 24A), indicating robust systemic T-cell activation. Consistent with this, *ex vivo* restimulation of splenocytes with TEVs induced a significant increase in IFN-γ^+ $CD8^+$ T cells (Supplementary Fig. 24B), confirming functional antigen-specific responses. This systemically activated, tumor-specific immunity further suppressed metastasis**,** as evidenced by examination of the lungs, which showed significantly fewer and smaller metastatic nodules in the TCG/FK_{12}F and TCG/FK_{12}F + aPD-1 groups compared to the PBS, aPD-1, and TCG alone groups (Fig. 5J, Supplementary Fig. 25). Collectively, these findings highlight the robust anti-metastatic potential of the TCG/FK_{12}F vaccine, underscoring its efficacy not only in local tumor control but also in preventing metastatic spread in a range of cancer models.

Personalized TCG/FK_{12}F vaccine effectively prevents tumor recurrence after surgery

Tumor recurrence is very common after surgery and significantly impacts patients' quality of life and prognosis. Recurrence may occur if surgery fails to completely remove the tumor, leaving behind minimal residual disease (MRD). To simulate this clinical situation, we constructed surgical resection models, including an RM-1 cell-based subcutaneous tumor resection model for prostate cancer and a 4T1 cell-based orthotopic tumor resection model for breast cancer. Mice inoculated with tumors underwent surgical excision after a period of time, leaving a few tumors to simulate residual lesions. The excised

tumors were used to extract TEVs to prepare personalized vaccines, which were subsequently infused back into the mice subcutaneously for treatment and monitoring of tumor recurrence (Fig. 6A). We performed relevant characterization of TEVs extracted from tumor tissues and verified the successful preparation of personalized TEVs (Supplementary Fig. 26A to D). As we can see from the RM-1 tumor resection model, although aPD-1 and TCG treatment delayed tumor recurrence in some degree, the anti-tumor effect was very limited and failed to enhance the survival rate of mice (Fig. 6B to D and Supplementary Fig. 27). In contrast, mice treated with the TCG/FK_{12}F vaccine demonstrated potent tumor suppression, with a survival rate of 25% at 90 days and up to 62.5% by combining with aPD-1.

We expanded the sample size and further replicated the experiment to obtain RM-1 tumor tissues from different groups for detection. Transcriptome sequencing analysis of the tumor tissue showed that gene expression upregulated by CG/FK_{12}F treatment was relatively limited (Fig. 6E). In contrast, TCG/FK_{12}F vaccine treatment resulted in the expression of a large number of immune-related genes within the tumor, including *Cd8a* and *Cxcr6*, suggesting that TEVs play a key role in the vaccine (Fig. 6F). This is similarly corroborated by the heat maps of gene expression in the three groups (Fig. 6G). Gene Ontology (GO) and Kyoto Encyclopedia of Genes and Genomes (KEGG) enrichment analysies of genes up-regulated in TCG/FK_{12}F showed that most of these genes act on immune-related pathways, such as T-cell proliferation and activation, cell killing, cytokine response, etc (Fig. 6H). Subsequent immune infiltration analysis further disclosed a marked increase in $CD8^+$ T-cell abundance in the TCG/FK_{12}F group compared to both the PBS and CG/FK_{12}F groups, indicative of enhanced antitumor immunity (Fig. 6I). Additionally, other anti-tumor immune cells, including DCs, NK cells, and Th1 cells, were also elevated in the TCG/FK_{12}F group. Consistently, the TCG/FK_{12}F vaccine showed significant efficacy in an orthotopic 4T1 breast cancer resection model, significantly inhibiting tumor recurrence (Fig. 6J and K). Accompanying flow cytometry analysis revealed a marked increase in IFN-γ^+ $CD8^+$ T cells (Supplementary Fig. 28), aligning with our earlier results and confirming its role in promoting antitumor T-cell responses. These results suggest that the personalized vaccine significantly inhibits postoperative tumor recurrence, and that this efficacy is enhanced by the combination of immune checkpoint inhibitors.

DISCUSSION

This study demonstrates that a personalized TEVs-based hydrogel vaccine induces robust immune activation, significantly augmenting T-cell infiltration into the TME and overcoming immunosuppressive barriers characteristic of cold tumors. Although conventional cancer vaccines show limited antitumor immune response[38,39] - mirrored in our experiments where TEVs with adjuvants alone demonstrated poor

efficacy due to rapid clearance and metabolic degradation - the $FK_{12}F$ hydrogel integration fundamentally addresses these limitations. Through electrostatic adsorption-mediated vaccine components incorporation, the hydrogel platform substantially prolongs immunotherapeutic agent retention and extends vaccine component duration compared to solution formulations. This engineered TCG/$FK_{12}F$ vaccine achieves *in situ* DC recruitment/activation, followed by DC migration to lymph nodes to initiate adaptive immunity. By programming spatiotemporal control over antigen/adjuvant biodistribution, our strategy overcomes the clearance encountered by traditional vaccines during their migration to the lymph nodes[40–42], ultimately generating a potent tumor-specific T-cell response through sustained immune stimulation.

These findings establish the mechanistic foundation for the enhanced therapeutic outcomes observed in TCG/$FK_{12}F$-treated tumor-bearing mice. Specifically, in the RM-1 prostate cancer model, TCG/$FK_{12}F$ vaccine synergized with aPD-1 to achieve significant tumor growth suppression and optimal survival rates. The vaccine's clinical potential is also underscored by its capacity to establish durable T-cell memory, as validated through tumor rechallenge experiments - coupled with superior survival benefits in both orthotopic and metastatic models, suggesting unprecedented efficacy in recurrence prevention. Consistent with these discoveries, our studies also demonstrated that the TCG/$FK_{12}F$ vaccine effectively enhanced T cell infiltration in TME, driving a critical shift from an immunologically cold into hot phenotypes. Most remarkably, the engineering of personalized cancer vaccines using TEVs isolated from surgically excised tumors exemplifies the platform's unparalleled adaptability, generating tumor-selective therapeutic efficacy through individualized antigen profiling. This precision strategy, specifically optimized for postoperative adjuvant therapy, harnesses autologous tumor antigens to maintain sustained antitumor immunity while overcoming traditional vaccine limitations, thereby substantially reducing recurrence risks through biologically personalized intervention.

Our experimental data confirm that TEVs, which are inherently rich in tumor-associated antigens, demonstrated potent immunostimulatory capacity. Unlike conventional EV vaccines requiring artificial neoantigen loading, this autologous TEV-based approach streamlines vaccine production through direct tumor-derived antigen utilization, simultaneously achieving personalized precision while eliminating complex antigen identification processes - thereby reducing manufacturing costs and shortening preparation timelines compared to synthetic platforms[43–45]. More importantly, the hydrogel delivery system establishes a subcutaneous antigen depot that significantly increasing the local concentration and extends bioactive persistence versus conventional administration, while circumventing rapid lymphatic

clearance through controlled release kinetics[46,47]. Mechanistically, TEVs outperformed tumor lysates by inducing greater DC activation and higher cytotoxic T-cell proliferation[48–51], likely due to preserved membrane topology and nano-scale dimensions that enhance antigen-presenting cell recognition[49,50,52]. In addition, compared to whole-cell therapies, TEVs do not have cellular structures, enhancing their safety profile. However, safety concerns regarding TEVs should not be overlooked, as they have been linked to tumor progression[53,54]. In our study, TEVs were loaded into a hydrogel and acted locally at the injection site, avoiding systemic circulation and thereby minimizing associated risks. The successful translation of this approach to the clinic, nevertheless, depends on several critical steps: comprehensive safety evaluation, precise dose optimization, the development of scalable GMP-compatible manufacturing protocols to ensure sufficient TEV yield, and a plan for ongoing therapeutic monitoring.

In summary, we develop a TEVs-based scaffold vaccine that elicits robust and durable antitumor immunity, demonstrating the system's high potency for personalized cancer immunotherapy. We show that the *in situ* formed TCG/$FK_{12}F$ hydrogel serves as a localized depot, prolonging retention of the vaccine components. This scaffold facilitates antigen-presenting DCs recruitment, enabling immature DCs to capture and process TEV antigens with CDA adjuvant support, thereby promoting DC maturation and eliciting robust tumor-specific $CD8^+$ T-cell activation to suppress progression in different tumor models. Notably, patient-specific TCG/$FK_{12}F$ vaccines tailored to individual tumors markedly prevent postoperative tumor recurrence. Our findings demonstrate that this rapidly customizable personalized vaccine induces potent and long-lasting antitumor immunity, exhibiting strong potential for clinical translation.

METHODS

Ethics statement

This study adhered to the ARRIVE (Animal Research: Reporting of *In Vivo* Experiments) guidelines. All the animal experiments were performed in accordance with the animal protocol approved by the Animal Ethics Committee at Shanghai Jiao Tong University (approval number: A2024071). The maximal tumor size permitted by the ethics committee was 2000 mm^3, and we confirm that this maximal tumor size was not exceeded in any experiment.

The human prostate tissues collection in this study was approved by the Research Ethics Committee of the Renji Hospital, Shanghai Jiao Tong University School of Medicine (approval number: KY2022-

136A). Written informed consent was obtained from all patients prior to the collection and use of human prostate tissue samples.

Study design

The objective of this study was to develop a TEVs-based personalized hydrogel vaccine for cancer immunotherapy. Using multiple murine tumor models, the efficacy of the TCG/$FK_{12}F$ vaccine in eliciting a robust antitumor immune response and suppressing tumor progression was validated. All experiments were repeated, with strict control of variables and standardized procedures to ensure consistent results across groups. Mice in the control and experimental groups were age- and sex-matched, and cage randomization was applied during group allocation.

Materials

GM-CSF was purchased from peprotech. CDA (2'3'-c-diAM $(PS)_2$(Rp,Rp)) was purchased from InvivoGen. Cy7-labelled CDA was purchased from Biolog Life Science Institute. All of the other chemicals were purchased from Sigma-Aldrich and used without any purification.

Cell lines

The RM-1-luc and 4T1-luc cell lines were donated by Renji hospital Shanghai Jiao Tong university school of medicine. The RM-1-luc cell line was cultured in DMEM (Gibco) supplemented with 10% fetal bovine serum (Gibco) and 1% penicillin/streptomycin (Gibco). The 4T1-luc cell line was cultured in RPMI-1640 medium (Gibco) supplemented with 10% fetal bovine serum (Gibco) and 1% penicillin/streptomycin (Gibco). All the cells were cultured in a constant temperature incubator at 37 °C with 5% CO_2 supply and routinely tested for mycoplasma.

Animals

Male C57BL/6 and femal BALB/c mice (aged 6-8 weeks; LINGCHANG Biotech) were maintained on a 12-hour light-dark cycle with unrestricted access to food and water.

TLs and TEVs extraction

Tumor tissues were divided into two portions for processing. One portion was homogenized and lysed on ice for 30 minutes in a lysis buffer containing protease inhibitors. The lysate was then centrifuged at 14,000 g for 20 minutes at 4 °C, and the supernatant was collected as TLs. The other portion of tumor tissue was minced and incubated at 37°C for 30 minutes in tissue isolation buffer, prepared with RPMI-1640 medium, collagenase D, and DNAse I. The mixture was filtered through a 70 μm membrane,

followed by sequential centrifugation at 2000 g and 10,000 g for 20 minutes each at 4 °C. The final supernatant was filtered through a 0.22 μm membrane, and TEVs were isolated by ultracentrifugation at 120,000 g for 70 minutes twice at 4°C. For tumor cell cultures, the medium was replaced with exosome-free serum medium at an appropriate time before collection. The medium was then centrifuged sequentially at 1,000 g for 10 minutes and at 10,000 g for 20 minutes at 4°C. The supernatant was filtered through a 0.22 μm membrane, and the filtrate was subjected to two rounds of ultracentrifugation at 120,000 g for 70 minutes each at 4°C to isolate TEVs.

Western blot

TLs and TEVs were lysed in RIPA lysis buffer (Beyotime), and protein concentration was quantified by BCA Protein Assay (Thermo Fisher Scientific). Equal amounts of protein were separated using a 10% SDS-PAGE gel and transferred onto 0.45 μm PVDF membranes (Millipore). The membranes were blocked with 5% BSA in TBST and incubated overnight at 4°C with specific primary antibodies. Afterward, appropriate secondary antibodies were applied, followed by detection using an ECL system (Tanon). See the source file for the uncropped scan blots.

Preparation of TCG/$FK_{12}F$

The polypeptide sequence FK12 (FKFEFKFEGRGD) was synthesized by peptide synthesizer. Verification of purity and molecular weight by HPLC and MS. To obtain self-assembled $FK_{12}F$, FK12 was directly dissolved in deionized water to reach a concentration of 15 mM and aged for 24 h at room temperature. The morphology of nanofibers was confirmed by transmission electron microscopy (Hitachi). The TCG/$FK_{12}F$ solution was prepared by adding 50 μg TEVs, 20 μg CDA and 2 μg GM-CSF to the $FK_{12}F$ solution. After vortexing, the mixed solution was incubated at 37 ℃ for 30 minutes. For *in vivo* imaging, CDA-Cy7 and TEVs-DIR was used.

Solution to hydrogel transition behavior

Add 20 μl of 10× PBS to 180 μl of 15 mM $FK_{12}F$ or TCG/$FK_{12}F$ solution, followed by vortexing. The transition of solution to hydrogel was observed by inverted-vial method.

***In vivo* hydrogel degradation**

The $FK_{12}F$ solution (15 mM, 200 μl) was injected into the back of C57BL/6 mice. After specified time intervals, the mice were euthanized, and the status of the remaining hydrogel in each mouse was recorded.

Hydrogel release studies

The in vitro release study was conducted at 37 °C in PBS. The release of CDA was analysed using HPLC. The release of GM-CSF was analysed using GM-CSF ELISA kit (Thermo Fisher Scientific). To evaluate the *in vivo* release of CDA and TEVs, Cy7-labeled CDA and DIR-labeled TEVs were injected subcutaneously into mice by free and TCG/$FK_{12}F$ loading, respectively. Fluorescence images were captured at predetermined time points using an IVIS Spectrum imaging system (Perkin Elmer).

In vivo tumor models and treatment

For subcutaneous model, 2.5×10^6 RM-1 cells were inoculated in male C57BL/6 mice with right flank. When the subcutaneous tumor volume reached 100-150 mm^3, the tumor-bearing mice were randomly grouped and then treated in different groups. Treatments included i.h. injected with PBS, CG/$FK_{12}F$, TCG or TCG/$FK_{12}F$ (50 μg TEVs, 20 μg CDA and 2 μg GM-CSF per mouse, 200 μl) on the contralateral side of the tumor, and intraperitoneal injections of aPD-1 (100 μg per mouse, 100 μl). For the prostate orthotopic model, 1×10^5 RM-1-luc cells were inoculated in male C57BL/6 prostate lobes. For the metastatic model, 1×10^5 4T1-luc cells were injected into female BALB/c through the left ventricle. After 5 days, Tumor-bearing mice from these two tumor models were randomly divided into five groups and received different treatments Treatments included i.h. injected with PBS, TCG or TCG/$FK_{12}F$ (50 μg TEVs, 20 μg CDA and 2 μg GM-CSF per mouse, 200 μl), and intraperitoneal injections of aPD-1 (100 μg per mouse, 100 μl). For the breast cancer orthotopic model, 1×10^6 4T1-luc cells were inoculated into the fat pad between the fourth and fifth nipple in female BALB/c mice. When the tumor volume reached 300-500 mm^3, the tumor-bearing mice underwent surgical removal of the tumors, with about 10% of the tumor remaining, and were then randomized into five groups to receive different treatments. Treatments included i.h. injected with PBS, TCG or TCG/$FK_{12}F$ (50 μg TEVs, 20 μg CDA and 2 μg GM-CSF per mouse, 200 μl) on the contralateral side of the tumor, and intraperitoneal injections of aPD-1 (100 μg per mouse, 100 μl). The tumor size was measured every 2 days. The tumor volume was calculated using the formula V = (major axis) × (minor axis)^2/2. For prostate orthotopic and breast metastasis models, tumor progression was monitored by the IVIS spectral imaging system (Perkin Elmer). Mice were euthanized when the subcutaneous tumor volume exceeded 2000 mm^3 or the weight loss exceeded 20%. For rechallenge experiment, mice with long-term survival were inoculated with 5×10^5 RM-1 cells on the opposite flank to develop new tumors.

Flow cytometry

Lymphocytes were extracted from peripheral blood, gel, lymph node, spleen, or tumor tissue, respectively, to prepare single-cell suspensions. Cells were stained with fluorescence-labeled antibodies following the

manufacturer's instructions. The samples were then analyzed on a LSRFortessa instrument (BD Biosciences), and data were analysed using FlowJo. Antibodies against CD45 (30-F11), CD3 (17A2), CD11c (N418), CD80 (16-10A1), CD86 (GL-1), CD197 (4B12), CD4 (RM4-5), CD8α(53-6.7), IFN-γ (XMG1.2), CD44 (IM7) and CD62L (MEL-14) were purchased from Biolegend.

Enyzme-linked immunospot assay

Splenocytes from RM-1 tumor-bearing mice were collected for restimulation with TEVs. 10 days after i.h. injected with PBS, CG/$FK_{12}F$, TCG or TCG/$FK_{12}F$, spleens were collected and spleen cells were extracted. Splenocytes (1×10^5) were stimulated for 24 h with 1 μg/well TEVs (from RM-1 cells). Cells were subsequently assayed for IFN-γ by Elispot kit (Mabtech) and spot counts using instrument (BD Biosciences).

***In vivo* T-cell depletion**

To deplete $CD4^+$ T and $CD8^+$ T cells, tumor-bearing mice were i.p. injected with anti-CD4 (clone GK1.5, BioXcell), anti-CD8-α (clone 2.43, BioXcell) or isotype (RatIgG1, BioXcell) antibodies. Antibodies were administered with an initial dose of 400 mg 1 day prior to treatment, followed by 200 mg every 3 days. Flow cytometry analysis of peripheral blood mononuclear cells confirmed the depletion of $CD4^+$ T cells and $CD8^+$ T cells.

Transcriptome data analysis

Differential gene expression analysis was performed in R (v4.4.1) using the DESeq2 (v1.44.0) package, with genes considered significantly differentially expressed at an adjusted p value < 0.05. Functional enrichment analyses were conducted using clusterProfiler (v4.12.6). Visualization of differentially expressed genes was generated using ggplot2 (v3.5.1) for volcano plots and pheatmap (v1.0.12) for hierarchical clustering heatmaps. Immune cell infiltration was estimated from bulk RNA-seq data using the CIBERSORT algorithm, which infers the relative abundance of immune cell subset within the tumor microenvironment.

Statistics and Reproducibility

Statistical analysis was conducted using GraphPad Prism 9. Data are presented as mean ± SEM. Statistical significance between two groups was determined using two-tailed unpaired t-tests. Statistical significance between multiple groups was determined using one-way ANOVA. Survival analysis was performed with Kaplan–Meier curves and evaluated using two-sided log-rank (Mantel–Cox) tests. No statistical method

was used to predetermine sample size. The Investigators were not blinded to allocation during experiments and outcome assessment.

Data Availability

The RNA sequencing data have been deposited in the NCBI Sequence Read Archive (SRA) under accession number PRJNA1330898 [https://www.ncbi.nlm.nih.gov/bioproject/PRJNA1330898]. All other data supporting the findings of this study are included in the main article, supplementary information or source data file. Source data are provided with this paper.

References

1. Kang, S. *et al.* Engineered IL-7 synergizes with IL-12 immunotherapy to prevent T cell exhaustion and promote memory without exacerbating toxicity. *Sci. Adv.* **9**, eadh9879 (2023).
2. Ben-Akiva, E., Chapman, A., Mao, T. & Irvine, D. J. Linking vaccine adjuvant mechanisms of action to function. *Sci. Immunol.* **10**, eado5937 (2025).
3. Kirchhammer, N., Trefny, M. P., Auf der Maur, P., Läubli, H. & Zippelius, A. Combination cancer immunotherapies: Emerging treatment strategies adapted to the tumor microenvironment. *Sci. Transl. Med.* **14**, eabo3605 (2022).
4. Lin, M. J. *et al.* Cancer vaccines: the next immunotherapy frontier. *Nat. Cancer* **3**, 911–926 (2022).
5. Dolton, G. *et al.* Targeting of multiple tumor-associated antigens by individual T cell receptors during successful cancer immunotherapy. *Cell* **186**, 3333–3349.e27 (2023).
6. Sahin, U. & Türeci, Ö. Personalized vaccines for cancer immunotherapy. *Science* **359**, 1355–1360 (2018).
7. Peri, A. *et al.* The landscape of T cell antigens for cancer immunotherapy. *Nat. Cancer* **4**, 937–954 (2023).
8. Chesney, J. A. *et al.* Randomized, double-blind, placebo-controlled, global phase III trial of talimogene laherparepvec combined with pembrolizumab for advanced melanoma. *J. Clin. Oncol.* **41**, 528–540 (2023).
9. Liang, F. *et al.* Vaccine priming is restricted to draining lymph nodes and controlled by adjuvant-mediated antigen uptake. *Sci. Transl. Med.* **9**, eaal2094 (2017).
10. Roth, G. A. *et al.* Designing spatial and temporal control of vaccine responses. *Nat. Rev. Mater.* **7**, 174–195 (2022).
11. Xia, H. *et al.* Computational prediction of MHC anchor locations guides neoantigen identification and prioritization. *Sci. Immunol.* **8**, eabg2200 (2023).

12. Li, J. *et al.* The screening, identification, design and clinical application of tumor-specific neoantigens for TCR-T cells. *Mol. Cancer* **22**, 141 (2023).
13. Pearlman, A. H. *et al.* Targeting public neoantigens for cancer immunotherapy. *Nat. Cancer* **2**, 487–497 (2021).
14. Manno, M., Bongiovanni, A., Margolis, L., Bergese, P. & Arosio, P. The physico-chemical landscape of extracellular vesicles. *Nat. Rev. Bioeng.* **3**, 68–82 (2025).
15. Tkach, M. & Théry, C. Communication by Extracellular Vesicles: Where we are and where we need to go. *Cell* **164**, 1226–1232 (2016).
16. Cocozza, F., Grisard, E., Martin-Jaular, L., Mathieu, M. & Théry, C. Snapshot: extracellular vesicles. *Cell* **182**, 262–262.e1 (2020).
17. Naseri, M., Bozorgmehr, M., Zöller, M., Pirmardan, E. R. & Madjd, Z. Tumor-derived exosomes: the next generation of promising cell-free vaccines in cancer immunotherapy. *Oncoimmunology* **9**, 1779991 (2020).
18. Zhou, W. *et al.* Exosomes derived from immunogenically dying tumor cells as a versatile tool for vaccination against pancreatic cancer. *Biomaterials* **280**, 121306 (2022).
19. Wiklander, O. P. B., Brennan, M. Á., Lötvall, J., Breakefield, X. O. & Andaloussi, S. E. Advances in therapeutic applications of extracellular vesicles. *Sci. Transl. Med.* **11**, eaav8521 (2019).
20. Zhang, C. *et al.* Tissue-derived extracellular vesicles: Isolation, purification, and multiple roles in normal and tumor tissues. *Life Sci.* **321**, 121624 (2023).
21. Han, J. *et al.* Novel personalized cancer vaccine using tumor extracellular vesicles with attenuated tumorigenicity and enhanced immunogenicity. *Adv. Sci.* **11**, e2308662 (2024).
22. Han, L. *et al.* Removing the stumbling block of exosome applications in clinical and translational medicine: expand production and improve accuracy. *Stem Cell Res. Ther.* **14**, 57 (2023).
23. Li, S. *et al.* Ex vivo expansion and hydrogel-mediated in vivo delivery of tissue-resident memory T cells for immunotherapy. *Sci. Adv.* **10**, eadm7928 (2024).
24. Barlek, M. H. *et al.* Systemic peptide amphiphile nanofiber delivery following subcutaneous injection. *Biomaterials* **303**, 122401 (2023).
25. Hernandez, A., Hartgerink, J. D. & Young, S. Self-assembling peptides as immunomodulatory biomaterials. *Front. Bioeng. Biotechnol.* **11**, 1139782 (2023).
26. Gong, N. *et al.* Enhancing in situ cancer vaccines using delivery technologies. *Nat. Rev. Drug Discov.* **23**, 607–625 (2024).

27. Liu, T. *et al.* Injectable nano-in-gel vaccine for spatial and temporal control of vaccine kinetics and breast cancer postsurgical therapy. *ACS Nano* **18**, 3087–3100 (2024).
28. Kim, J. *et al.* Injectable, spontaneously assembling, inorganic scaffolds modulate immune cells in vivo and increase vaccine efficacy. *Nat. Biotechnol.* **33**, 64–72 (2015).
29. Falcone, N. *et al.* Peptide hydrogels as immunomaterials and their use in cancer immunotherapy delivery. *Adv. Healthc. Mater.* **12**, e2301096 (2023).
30. Wang, F. *et al.* Supramolecular filament hydrogel as a universal immunomodulator carrier for immunotherapy combinations. *ACS Nano* **17**, 10651–10664 (2023).
31. Wang, F. *et al.* Tumour sensitization via the extended intratumoural release of a STING agonist and camptothecin from a self-assembled hydrogel. *Nat. Biomed. Eng.* **4**, 1090–1101 (2020).
32. Wang, F. *et al.* Supramolecular prodrug hydrogelator as an immune booster for checkpoint blocker-based immunotherapy. *Sci. Adv.* **6**, eaaz8985 (2020).
33. Fan, Q. *et al.* An implantable blood clot–based immune niche for enhanced cancer vaccination. *Sci. Adv.* **6**, eabb4639 (2020).
34. Shah, N. J. *et al.* A biomaterial-based vaccine eliciting durable tumour-specific responses against acute myeloid leukaemia. *Nat. Biomed. Eng.* **4**, 40–51 (2020).
35. Makarov, D. V., Loeb, S., Getzenberg, R. H. & Partin, A. W. Biomarkers for prostate cancer. *Annu. Rev. Med.* **60**, 139–151 (2009).
36. Reiter, R. E. *et al.* Prostate stem cell antigen: a cell surface marker overexpressed in prostate cancer. *Proc. Natl. Acad. Sci. U. S. A.* **95**, 1735–1740 (1998).
37. Wüstemann, T., Haberkorn, U., Babich, J. & Mier, W. Targeting prostate cancer: Prostate-specific membrane antigen based diagnosis and therapy. *Med. Res. Rev.* **39**, 40–69 (2019).
38. Le, D. T. *et al.* Results from a phase IIb, randomized, multicenter study of GVAX pancreas and CRS-207 compared with chemotherapy in adults with previously treated metastatic pancreatic adenocarcinoma (ECLIPSE study). *J. Am. Assoc. Cancer Res.* **25**, 5493–5502 (2019).
39. Hewitt, D. B. *et al.* A Phase 3 randomized clinical trial of chemotherapy with or without algenpantucel-L (hyperacute-pancreas) immunotherapy in subjects with borderline resectable or locally advanced unresectable pancreatic cancer. *Ann. Surg.* **275**, 45–53 (2022).
40. Batista-Duharte, A., Portuondo, D., Pérez, O. & Carlos, I. Z. Systemic immunotoxicity reactions induced by adjuvanted vaccines. *Int. Immunopharmacol.* **20**, 170–180 (2014).
41. Lynn, G. M. *et al.* In vivo characterization of the physicochemical properties of polymer-linked TLR agonists that enhance vaccine immunogenicity. *Nat. Biotechnol.* **33**, 1201–1210 (2015).

42. Francica, J. R. *et al.* Thermoresponsive polymer nanoparticles co-deliver RSV F trimers with a TLR-7/8 adjuvant. *Bioconjug. Chem.* **27**, 2372–2385 (2016).
43. Li, J. *et al.* Dendritic cell derived exosomes loaded neoantigens for personalized cancer immunotherapies. *J. Control. Release* **353**, 423–433 (2023).
44. Huang, L. *et al.* Engineered exosomes as an in situ DC-primed vaccine to boost antitumor immunity in breast cancer. *Mol. Cancer* **21**, 45 (2022).
45. Zhang, Y. *et al.* Complete remission of tumors in mice with neoantigen-painted exosomes and anti-PD-1 therapy. *Mol. Ther.* **31**, 3579–3593 (2023).
46. Meng, Y. *et al.* Extracellular vesicles-based vaccines: Emerging immunotherapies against cancer. *J. Control. Release* **378**, 438–459 (2025).
47. Shi, X. *et al.* Antitumor efficacy of interferon-γ-modified exosomal vaccine in prostate cancer. *The Prostate* **80**, 811–823 (2020).
48. Rao, Q. *et al.* Tumor-derived exosomes elicit tumor suppression in murine hepatocellular carcinoma models and humans in vitro. *Hepatol. Baltim. Md.* **64**, 456–472 (2016).
49. Liu, H. *et al.* Co-delivery of tumor-derived exosomes with alpha-galactosylceramide on dendritic cell-based immunotherapy for glioblastoma. *Cancer Lett.* **411**, 182–190 (2017).
50. Gu, X., Erb, U., Büchler, M. W. & Zöller, M. Improved vaccine efficacy of tumor exosome compared to tumor lysate loaded dendritic cells in mice. *Int. J. Cancer* **136**, E74–84 (2015).
51. Mahaweni, N. M. et al. Tumour-derived exosomes as antigen delivery carriers in dendritic cell-based immunotherapy for malignant mesothelioma. *J. Extracell. Vesicles* **2**, (2013).
52. Zitvogel, L. *et al.* Eradication of established murine tumors using a novel cell-free vaccine: dendritic cell-derived exosomes. *Nat. Med.* **4**, 594–600 (1998).
53. Peinado, H. *et al.* Melanoma exosomes educate bone marrow progenitor cells toward a pro-metastatic phenotype through MET. *Nat. Med.* **18**, 883–891 (2012).
54. Zhao, S. *et al.* Tumor-derived exosomal miR-934 induces macrophage M2 polarization to promote liver metastasis of colorectal cancer. *J. Hematol.* **13**, 156 (2020).

Acknowledgements: This study was supported by National Natural Science Foundation of China (82473851 to F.W., 82373358 and 82472142 to L.D., 82227801 to W.X., 82573527 to J.P.); National Key Research and Development Program of China (2025ZD01903300 and 2022YFC3501905 to F.W.); Major Natural Science Research Projects of Shanghai Municipal Education Commission (2023ZKZD23 to W.X.); Scientific Research Specialization on Post-market Clinical Research of Innovative Drugs of

National Healthcare Commission (WKZX2023CX100002 to J.P.); Shanghai Top Priority Research Center Project (2023ZZ02014 to W.X.); Shanghai High-level Local Universities Construction Program; Shanghai Rising-Star Program (23QA1405900 to L.D.); National Outstanding Young Physician of China (2022YQ014 to L.D.); Shanghai Rising-Star Young Medical Talents Program (to L.D.); Physician-Scientist Development Award from Shanghai Immune Therapy Institute (to L.D.); Shanghai Jiao Tong University 2030 Program (to L.D.).

Author contributions: J.P., F.W., L.D. and W.X. supervised the study; Q.C., C.J., F.W. and L.D. designed the experiments; X.D. constructed prostate orthotopic model and breast cancer metastasis model; M.T., Q.S., C.H. and Z.P. assisted in animal experiments; Q.C. completed analysis of transcriptome sequencing data; Q.C., F.W., L.D. and J.P. analyzed data and organized figures; J.P., W.X., L.D. and F.W. provided funding; Q.C., F.W., and J.P. wrote the manuscript. All authors revised the manuscript.

Competing interests: The authors declare that they have no competing interests.

Figure Legends

Fig. 1. **Verification of antigenicity of TEVs and schematic illustration of vaccine preparation and antitumor mechanism. A**, Schematic of TEVs and TLs obtained from prostate cancer patients. **B**, Western blot analysis for prostate cancer antigen markers (prostate acid phosphatase (PAP), prostate stem cell antigen (PSCA), and prostate-specific membrane antigen (PSMA)) expressed in TEVs and tumor lysates (TLs) (n = 3 independent experiments). **C**, Schematic illustration of TCG/$FK_{12}F$ vaccine preparation and its antitumor immunotherapeutic mechanism. Following subcutaneous injection, the *in situ* formed TCG/$FK_{12}F$ scaffold vaccine facilitated antigen-presenting DCs recruitment, enabling immature DCs to capture and process TEV antigens with CDA adjuvant support, thereby promoting DC maturation. These antigen-primed mature DCs then migrated to draining lymph nodes, eliciting robust tumor-specific CD8+ T-cell activation to suppress progression and prevent recurrence. Created in BioRender. 11, C. (2026) https://BioRender.com/y8vgrv0.

Fig. 2. Characterization of TCG/$FK_{12}F$ hydrogel vaccine. A, Representative transmission electron microscopy images of $FK_{12}F$ nanotubes (n = 3 independent experiments). **B**, Photographs of the solution-to-hydrogel transition of $FK_{12}F$ triggered by the addition of PBS. **C**, Rheomechanical curves of $FK_{12}F$. **D**, Representative transmission electron microscopy images of TEVs (n = 3 independent experiments). **E**, Particle size distribution of TEVs. **F**, Western blot analysis for extracellular vesicle markers (Flotillin-1,

CD63 and CD9) and contaminated protein (GM130) expressed in CLs and TEVs (n = 3 independent experiments). **G**, Zeta-potential analysis of $FK_{12}F$ solution, CG/$FK_{12}F$ (CDA and GM-CSF loaded into $FK_{12}F$) and TCG/$FK_{12}F$ (TEVs, CDA and GM-CSF loaded into $FK_{12}F$) (n = 5 independent experiments). **H**, Distribution of TEVs in $FK_{12}F$ photographed by confocal microscopy. **I**, Cumulative-release profile of CDA and GM-CSF from the TCG/$FK_{12}F$ incubated with PBS at 37 ℃ (n = 3 independent experiments). **J, K,** Fluorescence IVIS imaging and quantification of the *in vivo* retention of (**J**) CDA-Cy7 and (**K**) TEVs-DIR i.h. injected either in solution form or after loading into $FK_{12}F$ solutions (n = 3 mice per group). Data are mean ± SEM. Statistical significance in **J** and **K** was obtained by two-sided unpaired *t*-tests. Source data are provided as a Source Data file.

Fig. 3. TCG/$FK_{12}F$ vaccine recruits and activates DCs *in situ* and promotes their lymph node migration. **A-C**, Quantification using flow cytometry gating of DCs (**A**), $CD80^+CD86^+$ DCs (**B**) and $CCR7^+$ DCs (**C**) within the hydrogel in mice (n = 5 mice per group). **D-F**, Quantification using flow cytometry gating of (**D**) $CD80^+CD86^+$ DCs, (**E**) $CD4^+$ T cells and (**F**) $CD8^+$ T cells within the inguinal lymph nodes in mice (n = 5 mice per group). **G**, MHC class I mean fluorescence intensity (MFI) in gel-infiltrating DCs (n = 5 mice per group). **H**, MHC class I MFI in DCs from draining lymph nodes (n = 5 mice per group). **I**, Percentage of OVA antigen-presenting DCs determined by flow cytometry (n = 5 mice per group). **J,** Frequency of SIINFEKL–H-$2K^b$ $tetramer^+$ $CD8^+$ T cells in draining lymph nodes (n = 5 mice per group). **K**, Percentage of IFN-γ-producing $CD8^+$ T cells in splenocytes following *ex vivo* OVA peptide restimulation (n = 5 mice per group). **L,** Schematic depicting the mechanism by which the TCG/$FK_{12}F$ vaccine recruits and activates DCs in situ, thereby promoting the activation of tumor-specific T cells within the lymph nodes. Created in BioRender. 11, C. (2026) https://BioRender.com/cn9dqii. Data are mean ± SEM. Statistical significance in **A-K** was determined using one-way ANOVA. Source data are provided as a Source Data file.

Fig. 4. TCG/$FK_{12}F$ vaccine significantly inhibits tumor progression by promoting antigen-specific T cells infiltration and induces long-term immune memory. A, Experimental schematic of the RM-1 subcutaneous tumor treatment schedule, along with the timing for the rechallenge experiments. Mice that achieved long-term survival in all groups were rechallenged on day 60. **B**, Average tumor-growth kinetics of RM-1 tumor-bearing mice in different groups; n = 5 mice for PBS, aPD-1, CG/$FK_{12}F$ and TCG, and n = 8 mice for TCG/$FK_{12}F$ and TCG/$FK_{12}F$+aPD-1. The curves were plotted until the death of the first mice. **C**, Survival curves of different treatment groups. **D**, **E,** Quantification using flow cytometry gating of (**D**) $CD8^+$ T cells and (**E**) $CD8^+$ IFN-γ^+ T cells in RM-1 subcutaneous tumors (n = 5 mice per group).

F, Tumor tissue cytokines heatmap for each treatment group (n =3 mice per group). **G**, ELISPOT images showing IFN-γ spots from re-stimulated splenocytes in different groups (n = 3 mice per group). **H**, Quantification of the spots (n = 3 mice per group). **I**, Average tumor-growth kinetics of RM-1 tumor-bearing mice locally treated with TCG/$FK_{12}F$ along with depletion of $CD4^+$ T cells and $CD8^+$ T cells (n = 5 mice per group). **J**, Average tumor-growth kinetics of RM-1 tumor bearing mice of the rechallenge experiments (n = 5 mice per group). **K**, Survival curves of the rechallenge experiments. **L**, **M,** Quantification using flow cytometry gating of (**L**) $CD8^+$ T_{cm} cells and (**M**) $CD8^+$ T_{em} cells in splenocytes of the rechallenged mice (n = 5 mice per group). Data are mean ± SEM. Data are mean ± SEM. Statistical significance in **B, D, E, H** and **I** was determined using one-way ANOVA. Statistical significance in **C** and **K** was determined using two-sided log-rank tests. Statistical significance in **J, L** and **M** was determined using two-sided unpaired *t*-test. Source data are provided as a Source Data file.

Fig. 5. TCG/$FK_{12}F$ vaccine significantly inhibits proliferation of orthotopic prostate cancer and metastasis of 4T1 breast cancer. A, Experimental schematic of the RM-1 orthotopic tumor treatment schedule. **B**, *In vivo* bioluminescence imaging of RM-1 tumors on days 5, 8, 11, 14, 17, and 20 after tumor inoculation. n = 5 mice for each group. **C**, Survival curves of different treatment groups. **D**, Photographs of tumors removed from each treatment group on day 15. **E**, CD8 immunohistochemistry and Granzyme B immunofluorescence of RM-1 orthotopic tumors in different treatment groups (n = 3 mice per group). **F**, Heatmap of cytokines in RM-1 orthotopic tumor tissue in different treatment groups (n = 3 mice per group). **G**, Schematic of the treatment schedule for the 4T1 metastatic tumor model; n=5 mice for each group. **H**, *In vivo* bioluminescence imaging of 4T1 tumors on days 7 and 15 after tumor inoculation. **I**, Survival curves of different treatment groups. **J**, Photographs and hematoxylin-eosin staining results of lungs excised from each treatment group on day 16 (n = 5 mice per group). Data are mean ± SEM. Statistical significance in **C** and **I** was determined using two-sided log-rank tests. Source data are provided as a Source Data file.

Fig. 6. Personalized TCG/$FK_{12}F$ vaccine inhibits RM-1 tumor recurrence after surgery. A, Schematic diagram of constructing a personalized therapeutic vaccine treatment after surgical resection of tumor. **B-I**, Results of treatment in the RM-1 subcutaneous tumor resection model; n=5 mice for PBS, aPD-1 and TCG, and n=8 mice for TCG/$FK_{12}F$ and TCG/$FK_{12}F$ + aPD-1. **B**, *In vivo* bioluminescence imaging of the RM-1 tumors on the day 27. **C**, Tumor growth curves of mice in each treatment group (n = 5 mice per group). **D**, Survival curves of different treatment groups. **E**, **F**, Differential gene expression volcano maps of (**E**) CG/$FK_{12}F$ vs PBS and (**F**) TCG/$FK_{12}F$ vs PBS in RM-1 tumors (n = 4 mice per

group). **G**, Heatmap of differential gene expression in PBS, CG/$FK_{12}F$ and TCG/$FK_{12}F$ treated groups. **H**, GOKEGG enrichment analysis of up-regulated differential genes in TCG/$FK_{12}F$ treated groups (n = 4 mice per group). **I**, Immune infiltration analysis in PBS, CG/$FK_{12}F$ and TCG/$FK_{12}F$ treated groups (n = 4 mice per group). **J**, **K**, Results of treatment in 4T1 breast cancer orthotopic resection model; n = 5 mice for each group. **J**, Tumor growth curves of mice in each treatment group. **K**, Photographs of tumors removed from each treatment group on day 30. Data are mean ± SEM. Statistical significance in **C** and **J** was determined using one-way ANOVA. Statistical significance in **D** was determined using two-sided log-rank tests. Differential gene expression analysis in **E** and **F** was performed using DESeq2. P values were adjusted for multiple comparisons. Source data are provided as a Source Data file.

Editor's summary:
Personalized vaccines show some potential in leveraging tumor-specific adaptive immunity for cancer therapy. Here this group reports an in-situ hydrogel vaccine serving as a sustained reservoir for a tumor-derived extracellular vesicle antigens for personalized cancer immunotherapy.

Peer review information: *Nature Communications* thanks Shuguang Tan, Theresa Whiteside and the other anonymous reviewer(s) for their contribution to the peer review of this work. A peer review file is available.

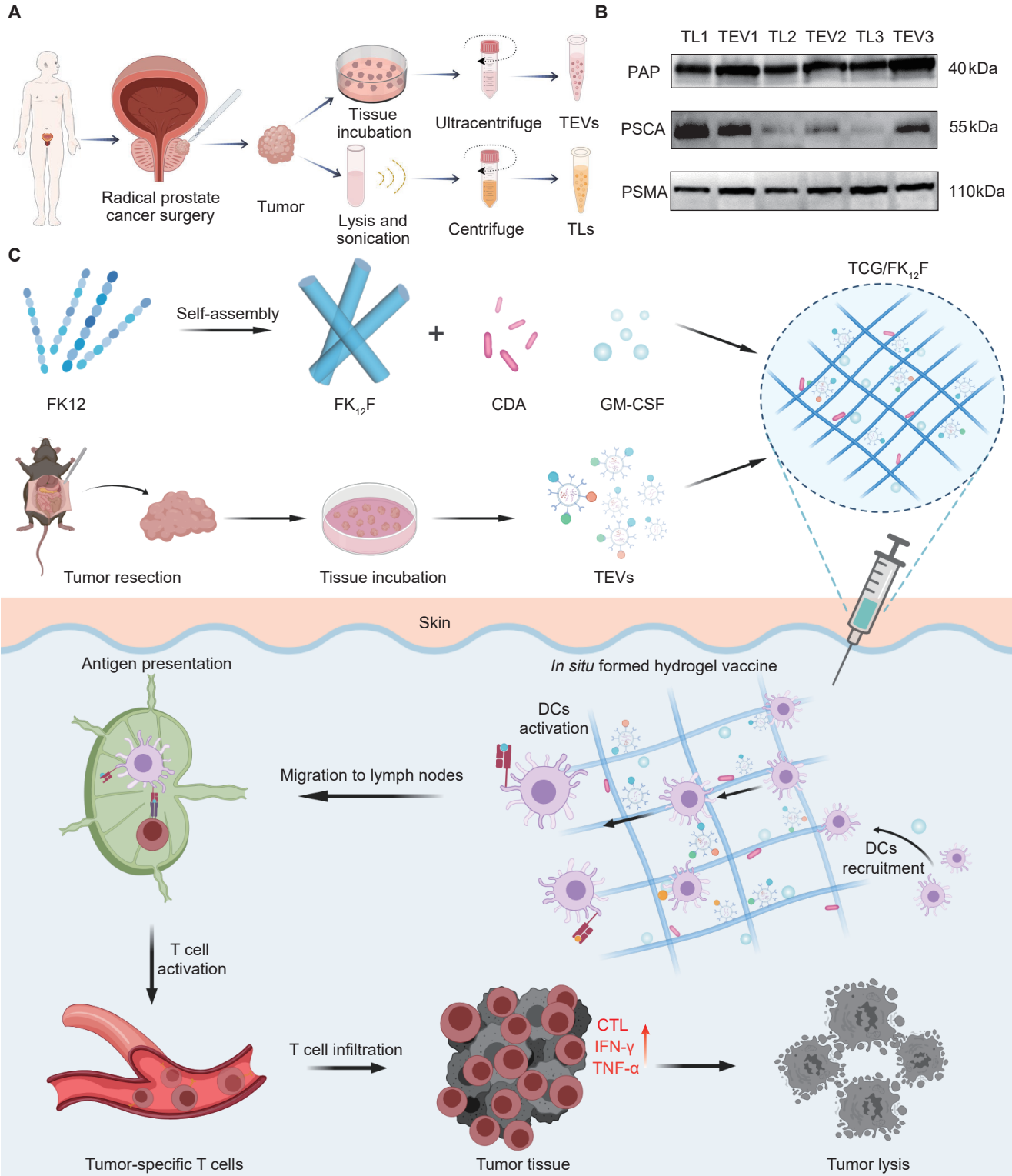
A
Radical prostate cancer surgery
Tumor
Tissue incubation
Ultracentrifuge
TEVs
Lysis and sonication
Centrifuge
TLs
B
TL1 TEV1 TL2 TEV2 TL3 TEV3
PAP
40 kDa
PSCA
55 kDa
PSMA
110 kDa
C
FK12
Self-assembly
FK12F
CDA
GM-CSF
TCG/FK12F
Tumor resection
Tissue incubation
TEVs
Skin
Antigen presentation
In situ formed hydrogel vaccine
DCs activation
Migration to lymph nodes
DCs recruitment
T cell activation
T cell infiltration
CTL
IFN-γ
TNF-α
Tumor-specific T cells
Tumor tissue
Tumor lysis

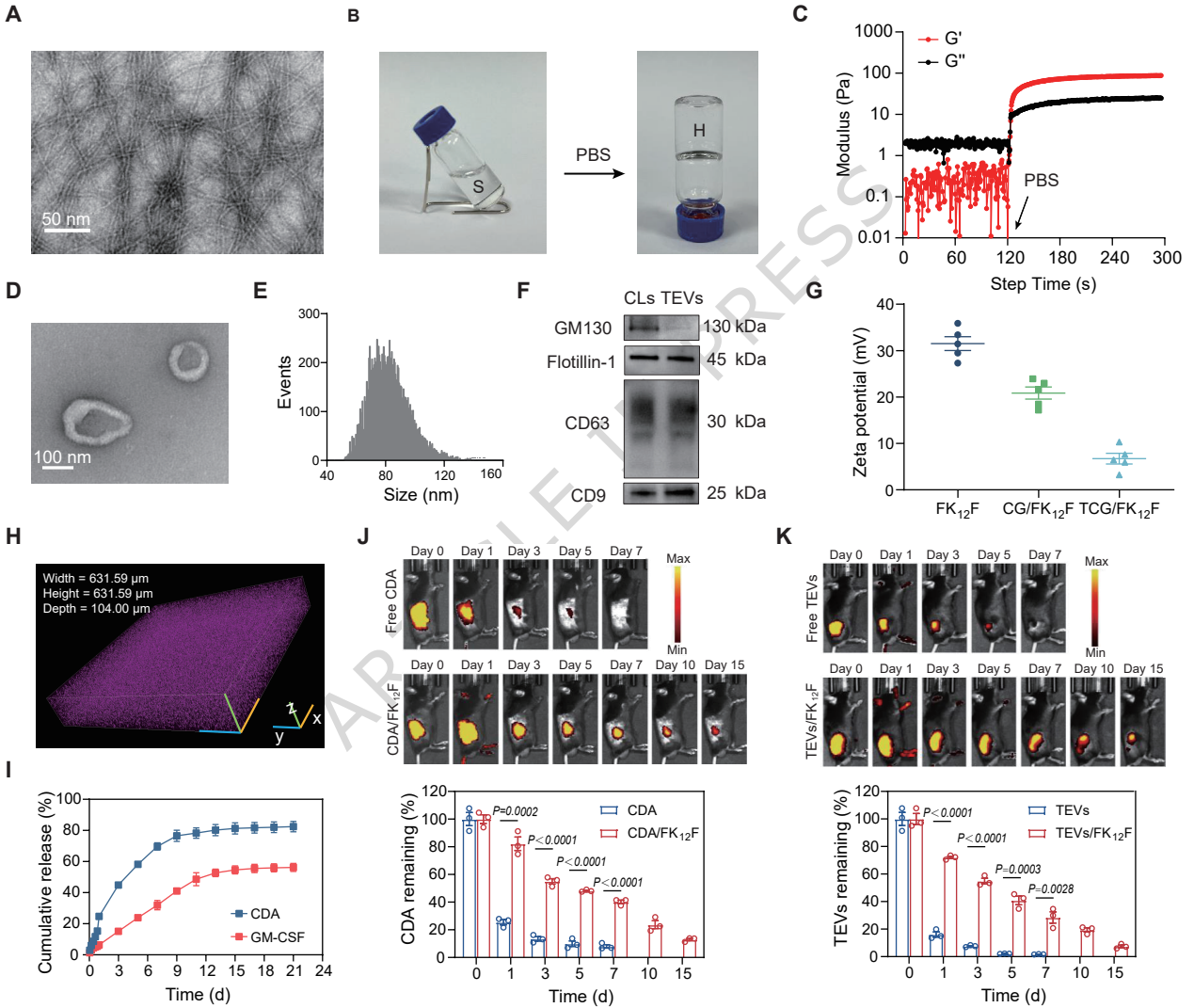

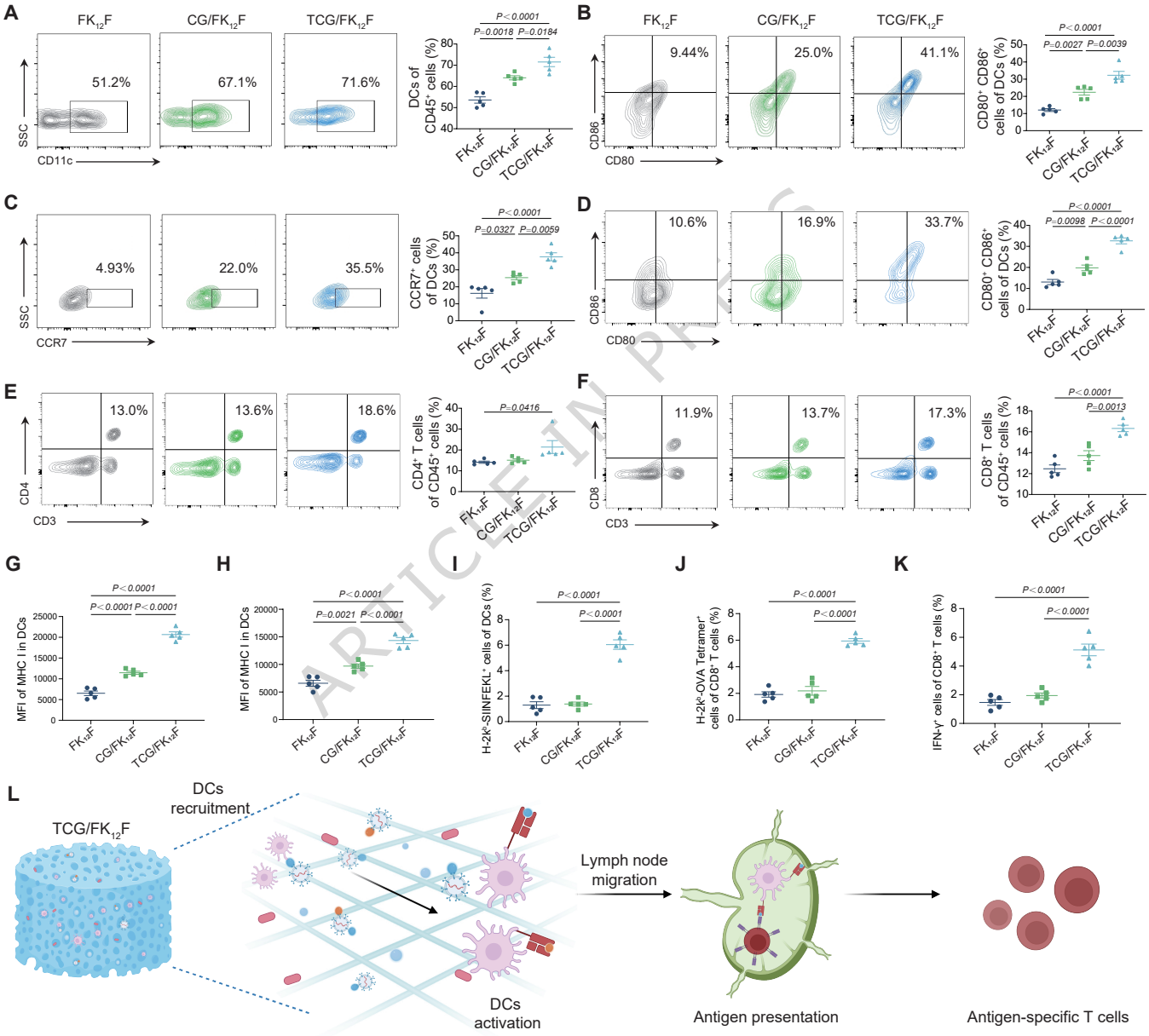
A
FK12F
CG/FK12F
TCG/FK12F
51.2%
67.1%
71.6%
SSC
CD11c
DCs of CD45+ cells (%)
P<0.0001
P=0.0018
P=0.0184
B
9.44%
25.0%
41.1%
CD86
CD80
CD80+ CD86+ cells of DCs (%)
P=0.0027
P=0.0039
C
4.93%
22.0%
35.5%
CCR7
CCR7+ cells of DCs (%)
P=0.0327
P=0.0059
D
10.6%
16.9%
33.7%
CD80+ CD86+ cells of DCs (%)
P=0.0098
P<0.0001
E
13.0%
13.6%
18.6%
CD4
CD3
CD4+ T cells of CD45+ cells (%)
P=0.0416
F
11.9%
13.7%
17.3%
CD8
CD3
CD8+ T cells of CD45+ cells (%)
P=0.0013
G
MFI of MHC I in DCs
H
MFI of MHC I in DCs
P=0.0021
I
H-2Kb-SIINFEKL+ cells of DCs (%)
J
H-2Kb-OVA Tetramer+ cells of CD8+ T cells (%)
K
IFN-γ+ cells of CD8+ T cells (%)
L
TCG/FK12F
DCs recruitment
DCs activation
Lymph node migration
Antigen presentation
Antigen-specific T cells

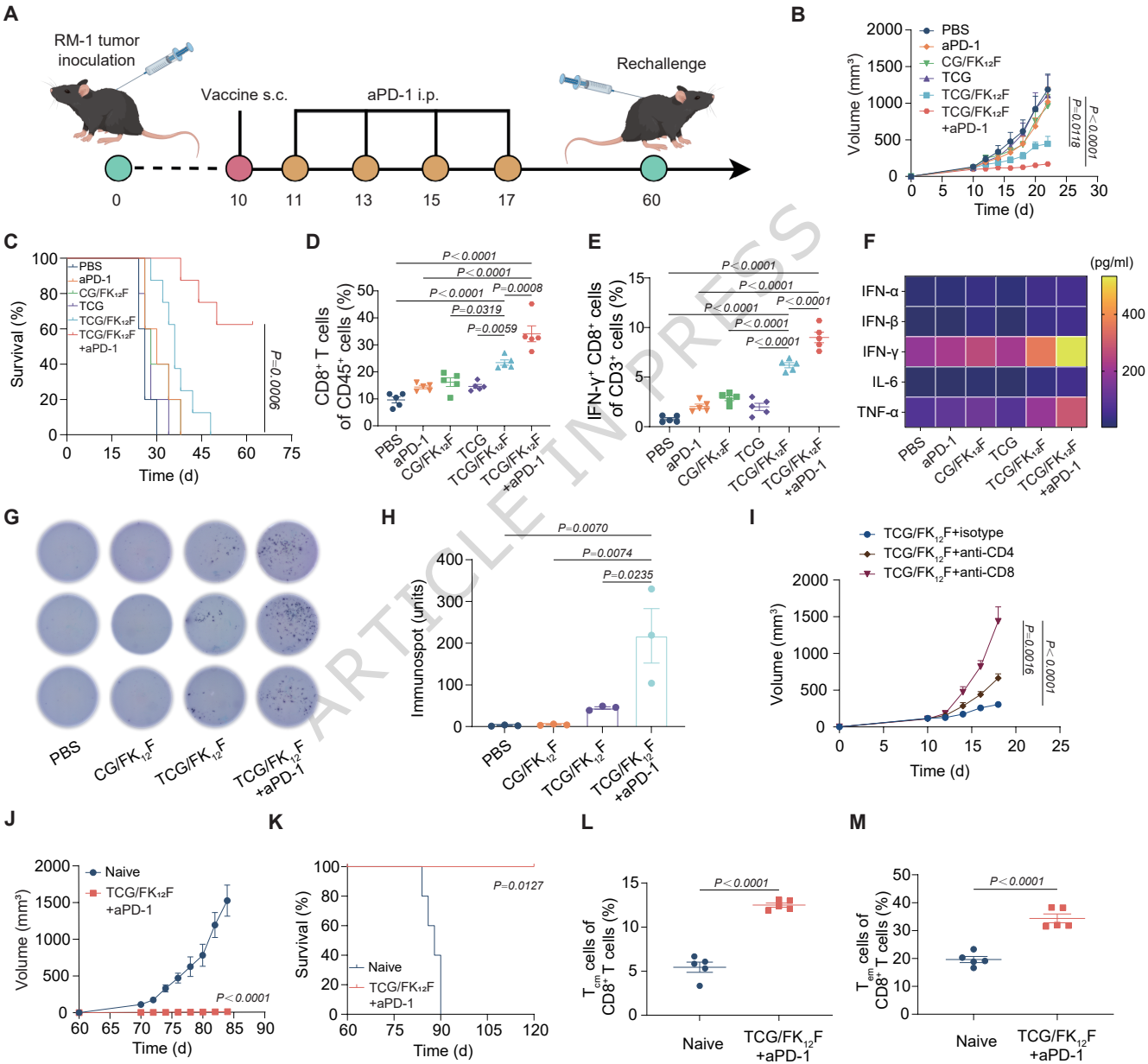

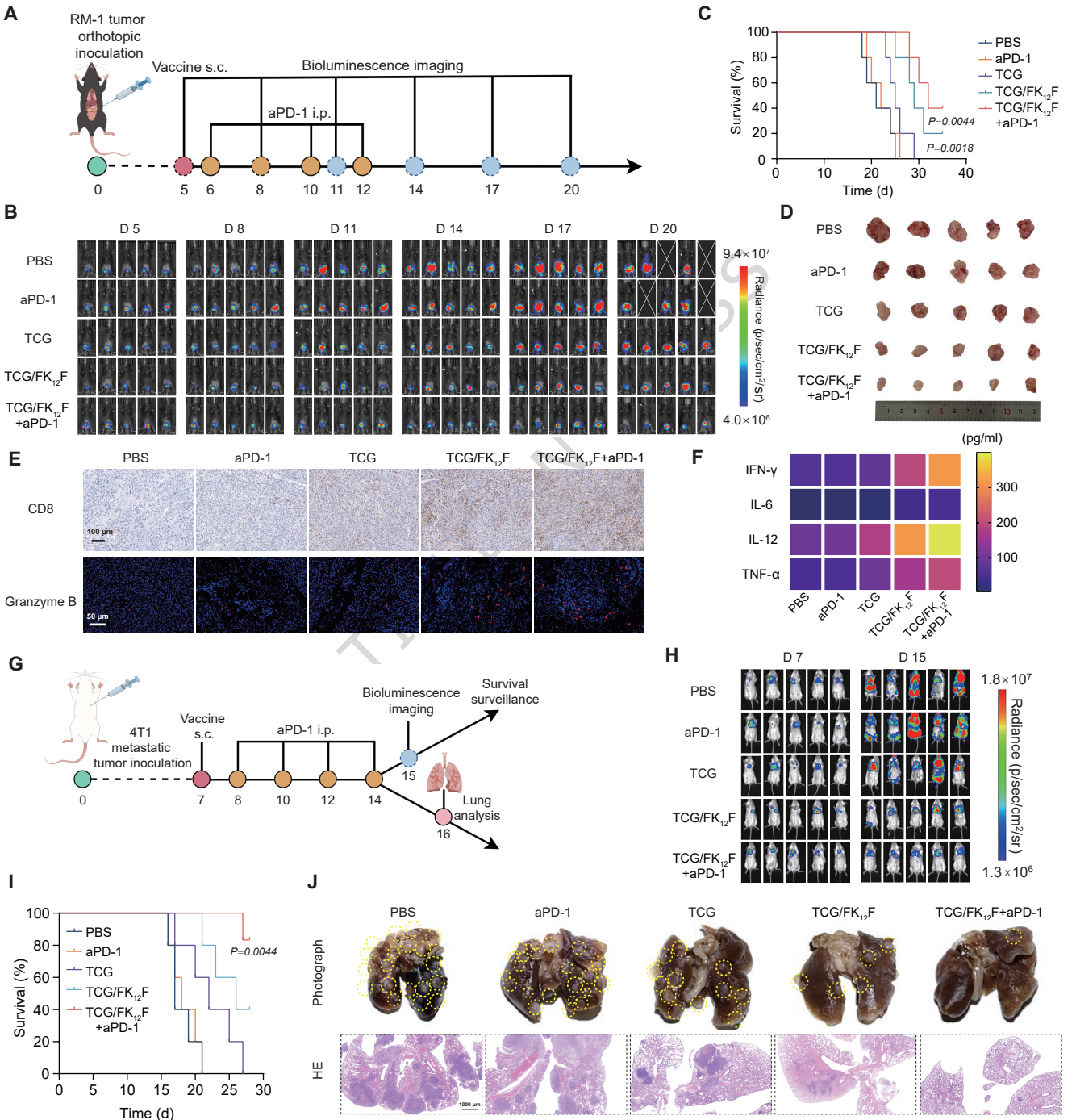
A
RM-1 tumor orthotopic inoculation
Vaccine s.c.
Bioluminescence imaging
aPD-1 i.p.
0 5 6 8 10 11 12 14 17 20
C
Survival (%)
Time (d)
PBS
aPD-1
TCG
TCG/FK12F
TCG/FK12F +aPD-1
P=0.0044
P=0.0018
B
D 5 D 8 D 11 D 14 D 17 D 20
PBS
aPD-1
TCG
TCG/FK12F
TCG/FK12F +aPD-1
9.4×10^7
4.0×10^6
Radiance (p/sec/cm²/sr)
D
PBS
aPD-1
TCG
TCG/FK12F
TCG/FK12F +aPD-1
E
PBS aPD-1 TCG TCG/FK12F TCG/FK12F+aPD-1
CD8
Granzyme B
100 μm
50 μm
F
(pg/ml)
IFN-γ
IL-6
IL-12
TNF-α
300
200
100
PBS aPD-1 TCG TCG/FK12F TCG/FK12F +aPD-1
G
4T1 metastatic tumor inoculation
Vaccine s.c.
aPD-1 i.p.
Bioluminescence imaging
Survival surveillance
Lung analysis
0 7 8 10 12 14 15 16
H
D 7 D 15
PBS
aPD-1
TCG
TCG/FK12F
TCG/FK12F +aPD-1
1.8×10^7
1.3×10^6
Radiance (p/sec/cm²/sr)
I
Survival (%)
Time (d)
PBS
aPD-1
TCG
TCG/FK12F
TCG/FK12F +aPD-1
P=0.0044
J
PBS aPD-1 TCG TCG/FK12,F TCG/FK12,F+aPD-1
Photograph
HE
1000 μm

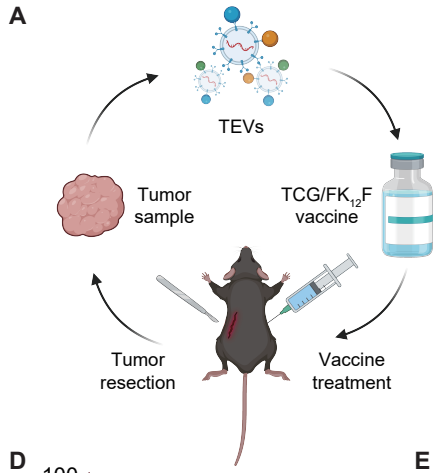
A
TEVs
Tumor sample
TCG/FK12F vaccine
Tumor resection
Vaccine treatment

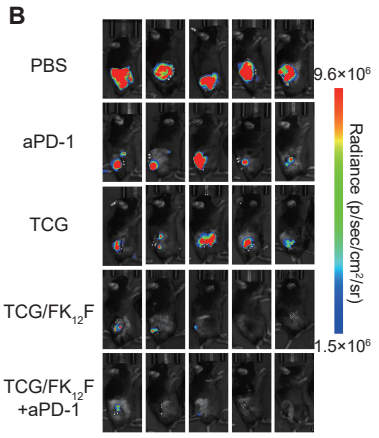
B
PBS
aPD-1
TCG
TCG/FK12F
TCG/FK12F +aPD-1
9.6×10⁶
1.5×10⁶
Radiance (p/sec/cm²/sr)

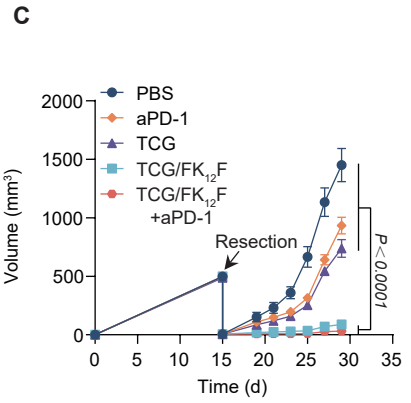
C
PBS
aPD-1
TCG
TCG/FK12F
TCG/FK12F +aPD-1
Resection
P<0.0001
Volume (mm³)
Time (d)

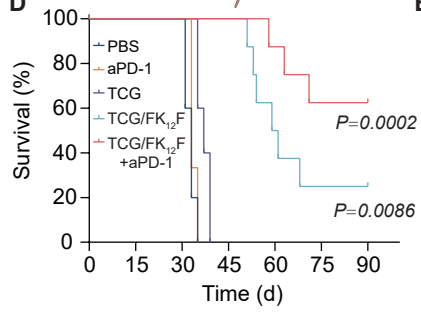
D
PBS
aPD-1
TCG
TCG/FK12F
TCG/FK12F +aPD-1
P=0.0002
P=0.0086
Survival (%)
Time (d)

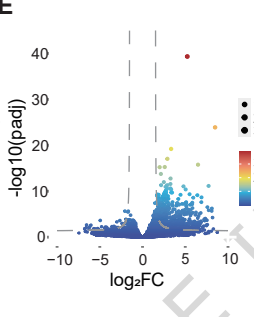
E
-log10(padj)
log2FC

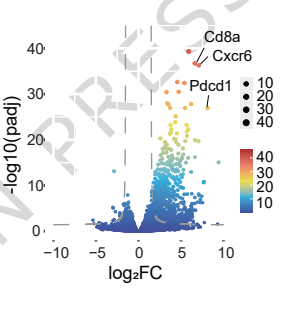
F
Cd8a
Cxcr6
Pdcd1
-log10(padj)
log2FC

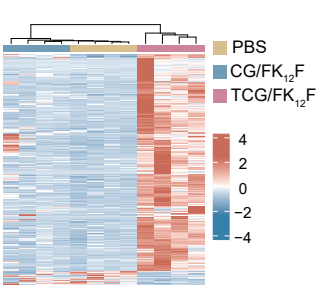
G
PBS
CG/FK12F
TCG/FK12F

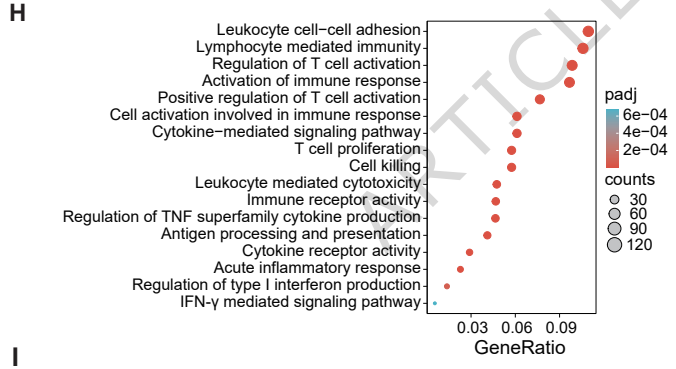
H
Leukocyte cell−cell adhesion
Lymphocyte mediated immunity
Regulation of T cell activation
Activation of immune response
Positive regulation of T cell activation
Cell activation involved in immune response
Cytokine−mediated signaling pathway
T cell proliferation
Cell killing
Leukocyte mediated cytotoxicity
Immune receptor activity
Regulation of TNF superfamily cytokine production
Antigen processing and presentation
Cytokine receptor activity
Acute inflammatory response
Regulation of type I interferon production
IFN-γ mediated signaling pathway
padj
counts
GeneRatio

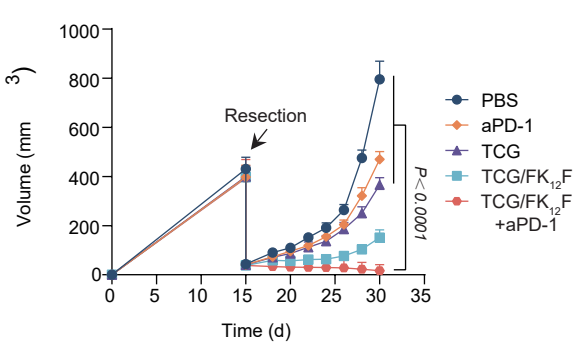
J
Resection
P<0.0001
Volume (mm³)
Time (d)
PBS
aPD-1
TCG
TCG/FK12F
TCG/FK12F +aPD-1

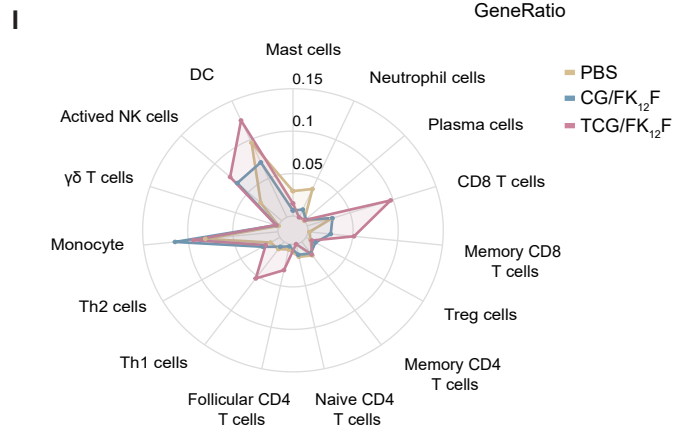
I
Mast cells
Neutrophil cells
Plasma cells
CD8 T cells
Memory CD8 T cells
Treg cells
Memory CD4 T cells
Naive CD4 T cells
Follicular CD4 T cells
Th1 cells
Th2 cells
Monocyte
γδ T cells
Actived NK cells
DC
PBS
CG/FK12F
TCG/FK12F

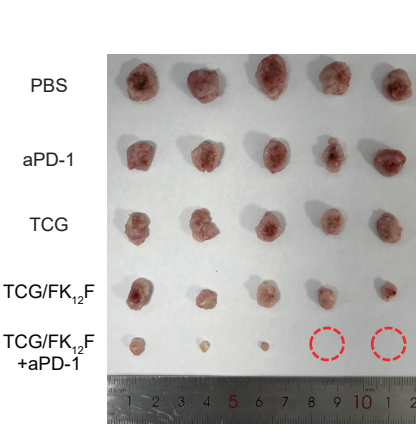
K
PBS
aPD-1
TCG
TCG/FK12F
TCG/FK12F +aPD-1